International Journal of Naval Architecture and Ocean Engineering 12 (2020) 85–101

Contents lists available at ScienceDirect

International Journal of Naval Architecture and Ocean Engineering

journal homepage: http://www.journals.elsevier.com/international-journal-of-naval-architecture-and-ocean-engineering/

Parametric studies on smoothed particle hydrodynamic simulations for accurate estimation of open surface flow force

Sangmin Lee, Jung-Wuk Hong*

Department of Civil and Environmental Engineering, Korea Advanced Institute of Science and Technology, 291 Deahak-ro, Yuseong-gu, Daejeon, 34141, Republic of Korea

ARTICLE INFO

Article history:
Received 8 March 2019
Received in revised form
18 July 2019
Accepted 23 July 2019
Available online 12 August 2019

Keywords:
Smoothed Particle Hydrodynamics (SPH)
Finite Element Method (FEM)
Fluid-structure Interaction (FSI)
Wave force
Smoothing length effect

ABSTRACT

The optimal parameters for the fluid-structure interaction analysis using the Smoothed Particle Hydrodynamics (SPH) for fluids and finite elements for structures, respectively, are explored, and the effectiveness of the simulations with those parameters is validated by solving several open surface fluid problems. For the optimization of the Equation of State (EOS) and the simulation parameters such as the time step, initial particle spacing, and smoothing length factor, a dam-break problem and deflection of an elastic plate is selected, and the least squares analysis is performed on the simulation results. With the optimal values of the pivotal parameters, the accuracy of the simulation is validated by calculating the exerted force on a moving solid column in the open surface fluid. Overall, the SPH-FEM coupled simulation is very effective to calculate the fluid-structure interaction. However, the relevant parameters should be carefully selected to obtain accurate results.

1. Introduction

There have been many accidental failures of offshore structures caused by the large forces of the excessively large waves or breaking waves (Vandiveret al., 1977; Bea et al., 1999; Chun et al., 2016; Cruz and Krausmann, 2008; Kettle, 2015). In fact, the wave forces are the most dominant external loads among the forces exerted onto the offshore structures, and therefore, the research for the calculation of wave force has remained as a field that requires more in-depth research. The accurate estimation of the wave force has been one of essential tasks to assess the safety of offshore structures. However, the excessive deformations, accompanied in a variety of fluid motions such as free-surface flows and wave break, have hindered accurate simulations of the waves in realistic conditions. In the Lagrangian formulation, the discretized domains, so-called elements, move with the material points. Therefore, each material point has a corresponding element mesh point. On the contrary, in the Eulerian formulation for the fluid mechanics, the mesh configuration is stationary and the material particles move through the mesh. The large motions and deformations of fluids of large waves make it difficult to describe the fluid behavior in the framework of the conventional Eulerian formulation. In order to calculate the fluid flows that have large changes in the configuration, the Arbitrary Lagrangian-Eulerian (ALE) formulation was developed. In the methodology, the mesh points move in accordance with the nature of the problem, and the condition is imposed by the solution algorithm (Bathe, 2006). However, the determination of the movement of the element nodes still makes difficulties in the calculation, and the capability to incorporate the domain changes is required to accommodate the fragmentation and merging of domains.

Meshless techniques have been developed to overcome the existing difficulties with mesh discretization. The methodology is classified into the local approach and nonlocal approaches. In the local approach, the field quantities are determined at each material point (Hong and Bathe, 2005; Arroyo and Ortiz, 2006), but in the nonlocal approach, the quantities are decided by reflecting all the values within the influence range. The Smoothed Particle Hydrodynamics (SPH) method considered as one of the famous nonlocal methodologies (Roque et al., 2011; Liu and Hong, 2012a, 2012b, 2012c) originally developed by Lucy, Gingold, and Monaghan for a three-dimensional astrophysical analysis using a lattice-free Lagrangian based particle method (Lucy, 1977; Gigold and Monaghan, 1977). The SPH method has been applied to a weakly compressible and inviscid fluid. For an incompressible fluid, a

* Corresponding author.
E-mail addresses: j.hong@kaist.ac.kr, jwhong@alum.mit.edu (J.-W. Hong).
Peer review under responsibility of Society of Naval Architects of Korea.

https://doi.org/10.1016/j.ijnaoe.2019.07.003

Moving Particle Semi-implicit (MPS) method developed by Koshizuka and Oka (1996) has been widely used in solving ocean engineering problems such as the interaction between an incompressible fluid and elastic structure (Khayyer et al., 2019), dam-breaking, and sloshing (Wang et al., 2019). Unlike Eulerian methods that require the mesh discretization, the SPH and MPS method calculate physical quantities between particles without requiring mesh information and use the field quantities at each node to describe smooth fields (Liu and Liu, 2010). Until the early 1990s, the SPH method had been mainly used for solid analyses. However, Monaghan extended the use to deal with the propagation of incompressible fluids of the free surface such as short wave, water column collapse, etc. (Monaghan, 1994). Monaghan and Kos then applied the methodology to analyze the isolated wave propagation patterns in aquariums and studied the run-up phenomenon of isolated waves by applying the technique to the beach (Monaghan and Kos, 1999).

In general, two kinds of SPH techniques have been used to analyze Fluid-structure Interaction (FSI) and free-surface fluid flows (Gotoh and Khayyer, 2018). First, fully-Lagrangian coupling method between weakly compressible SPH (WCSPH) or Incompressible SPH (ISPH) fluid and SPH based structure model have been used to analyze fluid-structure interaction (Gotoh and Khayyer, 2018; Khayyer et al., 2018a). Dalrymple and Knio proposed the way to construct the boundary walls using WCSPH particles in order to numerically investigate the two-dimensional dam-break problem (Dalrymple and Knio, 2001). Gómez-Gesteira and Dalrymple carried out three-dimensional analysis imposing the boundary conditions using WCSPH particles, so-called dynamic boundary particle method, and the obtained wave force was compared with the experiment data (Gómez-Gesteira and Dalrymple, 2004; Gómez-Gesteira et al., 2012; Gómez-Gesteira, 2013; Crespo et al., 2007). Khayyer et al. developed an enhanced ISPH-SPH coupling method for simulation of fluid-elastic structure interactions and the numerical model verified using various benchmark tests (Khayyer et al., 2018a). Next, by combining the Finite Element Method (FEM) and the SPH method, impact simulations were mainly performed. Attaway et al. defined the SPH node as the slave part and the surface of the finite element as the master part. By monitoring the penetration depth of the slave part, a contact constraint was defined to the nodes in order to prevent the penetration (Attaway et al., 1994). Johnson and Beissel proposed the normalized smoothing function algorithm to improve the accuracy of impact simulation using SPH (Johnson and Beissel, 1996). Vuyst et al. proposed a method of coupling a finite element to a smoothed particle using a node-to-node contact potential algorithm and verified using three numerical examples: a plate impact, water impact, and rod penetration (Vuyst et al., 2005). In Grimaldi et al., an automatic node-to-surface contact algorithm is used between the shell elements and the WCSPH particles to calculate the impact pressure and to predict the response of the structure under water impact (Grimaldi et al., 2011). Li et al. proposed a SPH-ALE coupling scheme to solve transient fluid-structure problems (Li et al., 2015). The stability of the numerical model is verified by means of some test cases such as the dam breaking and the impact of the tire on the surface of the water. Fourey et al. applied a Conventional Parallel Staggered (CPS) algorithm and a Conventional Sequential Staggered (CSS) algorithm to couple the fluid modeled by WCSPH and the structures discretized by finite elements (Fourey et al., 2017). As a result, the presented coupling methods effectively calculate the deformation of structures under hydrostatic pressure, the impact load of the elastic beam, and the water height during dam-break. Recently, Gotoh and Khayyer reviewed the state-of-the-art of smoothed particle hydrodynamics for coastal and ocean engineering and the WCSPH method has been widely applied for interactions between waves and floating bodies, solitary wave breaking, and second-order stoke wave propagation (Gotoh and Khayyer, 2018).

To accurately calculate the deformation of an elastic structure, various types of numerical researches have been performed with the use of SPH coupling and the dam-break experiment results have been compared with numerical results to evaluate the accuracies of various kinds of numerical techniques. However, the maximum dam-break force was often overestimated the fluid forces in accordance with the experiment results (Silvester and Cleary, 2006; Barreiro et al., 2013) and the parametric study of optimal values for fluid force using FEM-WCSPH coupling technique is rarely discussed.

The main purpose is to perform parametric studies in order to find optimum parameters to accurately calculate the wave forces acting on offshore structures. We investigate the effect of the initial particle spacing, smoothing length parameter, and time step scale factor through the simulation of hydrostatic pressure on an elastic plate and dam-break problem of which the experimental results are available. Then, we prove the improvement of accuracy in the fluid force estimation by solving a couple of numerical examples, using the optimal parameters.

2. Theory

The SPH method was developed for solving hydrodynamic problems expressed in the partial differential equations which have physical fields in integral equation forms. The continuum domain is discretized by discrete nodes, and the quantities at each node are influenced by surrounding material node, which renders the SPH method as a nonlocal numerical technique. The derivatives are obtained by differentiating the integrand functions and are smoothly continuous.

2.1. SPH formulation

Approximation of a function $f(x)$ is derived from the Dirac delta identity

$$\tilde{f}(\mathbf{x}) = \int_{\Omega} f(\mathbf{x}')\delta(\boldsymbol{x} - \boldsymbol{x}')d\boldsymbol{x}', \tag{1}$$

where x is the position vector, $\delta(\boldsymbol{x} - \boldsymbol{x}')$ is the Dirac delta function,

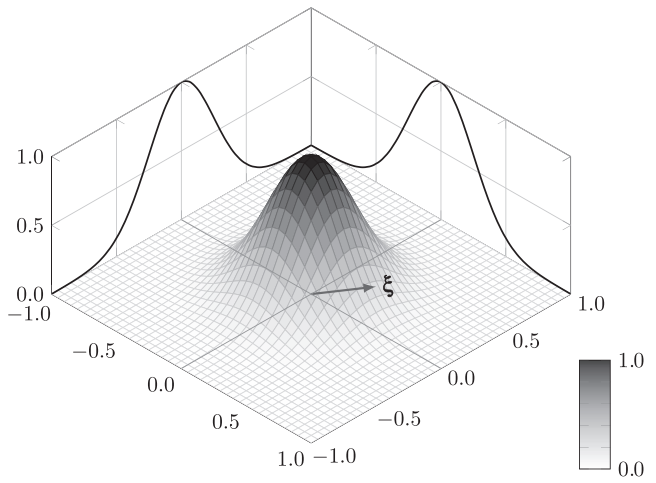

Fig. 1. Normalized smoothing function.

and Ω is the volume of the local space around the point x. By replacing the Dirac delta function with a smoothing function $W(\boldsymbol{x}-\boldsymbol{x}', h)$ of a finite support h, as shown in Fig. 1, the kernel approximation is expressed as

$$\tilde{f}(\boldsymbol{x}) = \int_{\Omega} f(\boldsymbol{x}')W(\boldsymbol{x}-\boldsymbol{x}', h)d\boldsymbol{x}'. \tag{2}$$

There exist a variety of smoothing functions of different orders in the polynomial expressions as (Cummins et al., 2012)

$$Cubic \;:\; W(\xi_{ij}, h) = \frac{1}{\pi h^3}\begin{cases} 1-\frac{3}{2}\xi_{ij}^2+\frac{3}{4}\xi_{ij}^3, & \text{for } \xi_{ij}\le 1 \\ \frac{1}{4}(2-\xi_{ij})^3, & \text{for } 1<\xi_{ij}\le 2 \\ 0, & \text{for } 2<\xi_{ij} \end{cases} \tag{3}$$

$$Quartic \;:\; W(\xi_{ij}, h) = \frac{1}{\pi h^3}\begin{cases} (2.5-\xi_{ij})^4-5(1.5-\xi_{ij})^4+10(0.5-\xi_{ij})^4, & \text{for } \xi_{ij}\le 0.5 \\ (2.5-\xi_{ij})^4-5(1.5-\xi_{ij})^4, & \text{for } 0.5<\xi_{ij}\le 1.5 \\ (2.5-\xi_{ij})^4, & \text{for } 1.5<\xi_{ij}\le 2.5 \\ 0, & \text{for } 2.5<\xi_{ij} \end{cases} \tag{4}$$

$$Wendland \;:\; W(\xi_{ij}, h) = \frac{7}{85.336\pi h^3}\begin{cases} (2-\xi_{ij})^4(1+2\xi_{ij}), & \text{for } 0\le\xi_{ij}\le 2.0 \\ 0, & \text{for } 2.0\le\xi_{ij} \end{cases} \tag{5}$$

where $\xi_{ij} = ||\mathbf{x}_I - \mathbf{x}_J||/h$, and the smoothing functions vanish with the compact supportness. It should be noted that the smoothing functions are normalized to render the volume to be a unity, and the magnitudes of the functions are always positive. In the commercial code LS-DYNA, the cubic smoothing function has been used for the SPH simulations.

2.2. Governing equations for SPH method

In SPH analysis, the continuity equation, as well as the conservation equations of linear momentum and energy, are expressed as follows:

$$\frac{D\rho}{Dt}+\rho\frac{\partial v^\beta}{\partial x^\beta}=0, \tag{6}$$

$$-\frac{Dv^\alpha}{Dt}+\frac{1}{\rho}\frac{\partial\sigma^{\alpha\beta}}{\partial x^\beta}+F^\alpha=0, \tag{7}$$

$$\frac{De}{Dt}-\frac{\sigma^{\alpha\beta}}{\rho}\frac{\partial v^\alpha}{\partial x^\beta}=0, \tag{8}$$

where ρ is the density, $\beta=\{x,y,z\}$, x^β are the coordinates, v^β are velocities, $\sigma^{\alpha\beta}$ are stresses, F^α is the body force normalized by the density, and e is the internal energy. By use of the kernel approximation, the SPH formulations for the continuity, momentum, and energy equations for the node i are expressed as

$$\frac{D\rho_i}{Dt}=\sum_{j=1}^{N} m_j v_{ij}^\beta\frac{\partial W_{ij}}{\partial x_i^\beta}, \tag{9}$$

$$\frac{Dv_i^\alpha}{Dt}=\sum_{j=1}^{N} m_j\left(\frac{\sigma_i^{\alpha\beta}}{\rho_i^2}+\frac{\sigma_j^{\alpha\beta}}{\rho_j^2}\right)\frac{\partial W_{ij}}{\partial x_i^\beta}+F_i^\alpha, \tag{10}$$

$$\frac{De_i}{Dt}=-\frac{1}{2}\sum_{j=1}^{N} m_j\left(\frac{\sigma_i^{\alpha\beta}}{\rho_i^2}+\frac{\sigma_j^{\alpha\beta}}{\rho_j^2}\right)v_{ij}^\beta\frac{\partial W_{ij}}{\partial x_i^\beta}, \tag{11}$$

where ρ_i is the density of the particle i, $v_{ij}(=v_i-v_j)$ are the relative velocities, $\sigma_i^{\alpha\beta}$ are the total stresses, and e is the specific internal energy. The total stresses $\sigma^{\alpha\beta}$ are decomposed into isotropic pressure P and the deviatoric viscous stresses as

$$\sigma^{\alpha\beta}=-P\delta^{\alpha\beta}+\tau^{\alpha\beta}, \tag{12}$$

where $\delta^{\alpha\beta}$ is the Kronecker delta and $\tau^{\alpha\beta}$ is the deviatoric viscous stresses. For Newtonian fluids, deviatoric stress can be defined as

$$\tau^{\alpha\beta}=2\mu\dot{\varepsilon}^{\alpha\beta}, \tag{13}$$

and where μ is the shear viscosity of the fluid and $\dot{\varepsilon}^{\alpha\beta}$ are the strain rates. In order to calculate the isotropic pressure P, it is required to have a relationship between the pressure and other material property variables. For this purpose, the equation of state (EOS) was developed (Hallquist, 2006). Among several types of equations of state, the Gruneisen equation has been widely used to describe the fluid motions in SPH. The EOS for compressible materials is expressed as (Boyd et al., 2000; Hallquist, 2007)

$$P=\frac{\rho_0 C^2\tilde{\mu}\left(1+\left(1-\frac{\gamma_0}{2}\right)\left(\frac{\rho}{\rho_0}-1\right)-\frac{a}{2}\tilde{\mu}^2\right)}{\left(1-(S_1-1)\left(\frac{\rho}{\rho_0}-1\right)-S_2\left(\frac{\rho_0}{\rho}\right)\left(\frac{\rho}{\rho_0}-1\right)^2-S_3\left(\frac{\rho_0}{\rho}\right)^2\left(\frac{\rho}{\rho_0}-1\right)^3\right)^2}+(\gamma_0+a\tilde{\mu})E, \tag{14}$$

and for expandable material it is written as

$$P=\rho_0 C^2\frac{\rho}{\rho_0}-1+\left(\gamma_0+a\left(\frac{\rho}{\rho_0}-1\right)\right)E, \tag{15}$$

where ρ_0 is the initial density, ρ is the current density, u_s is the cubic shock velocity, u_p is the fluid particle velocity, C is the intercept of

the $(u_s - u_p)$ curve, S_i $(i = 1, 2, 3)$ are the coefficients of the slope of the $(u_s - u_p)$ curve, E is the initial internal energy per unit volume, γ_0 is the Gruneisen gamma, a is the first order volume correction to γ_0, and $\tilde{\mu}$ is the volumetric parameter. The Gruneisen EOS parameters for water are listed in Table 1.

2.3. Solution procedures

In the solution procedures, velocity, density, internal energy, and coordinates are calculated at each time step. For the time integration, the leap-frog scheme is utilized (Libersky et al., 1993), which requires calculation of the velocities followed by other variables sequentially. The velocities at the $(1/2)^{\text{th}}$ step are calculated by

$$v_j^{\frac{1}{2}} = v_j^0 + \Delta t \left.\frac{dv_j}{dt}\right|_{k=0}, \tag{16}$$

where $v_j^{\frac{1}{2}}$ are velocities at 1/2 step, v_j^0 are the initial velocities, and $\left.\frac{dv_j}{dt}\right|_{k=0}$ are the time derivatives of the velocities. Further calculation at the $(k+1/2)^{\text{th}}$ step is obtained by

$$v_j^{k+\frac{1}{2}} = v_j^{k-\frac{1}{2}} + \Delta \left.\frac{dv_j}{dt}\right|_k. \tag{17}$$

The velocity at step k is interpolated by $v_j^k = 1/2\left(v_k^{k+\frac{1}{2}} - v_j^{k-\frac{1}{2}}\right)$, and the density, energy and the coordinates $(k+1)^{\text{th}}$ step are updated using the explicit integrations as follows

$$\rho_j^{k+1} = \rho_j^k + \Delta t \left.\frac{d\rho_i}{dt}\right|_k, \tag{18}$$

$$e_j^{k+1} = e_j^k + \Delta t \left.\frac{de_i}{dt}\right|_k, \tag{19}$$

$$x_j^{k+1} = x_j^k + \Delta t\, v_j^k, \tag{20}$$

where the change rates of the density and the energy are calculated from the discretized equations at each time step while the velocities are updated by Eq. (17). To ensure the stability of the calculation, the Courant-Friedrichs-Lewy (CFL) condition should be satisfied.

3. SPH-FEM coupling

To calculate the fluid force exerted on the structure, we use smoothed particle hydrodynamics (Hallquist, 2007) and finite element procedures (Bathe, 2006), which are widely used in engineering analysis. Contact algorithm is implemented to couple the finite element and the smoothed particles.

3.1. Contact algorithm

The contact algorithm is a function that determines the interaction between two different kinds of formulations. It can be used in collision analysis where one element hits another, or in the numerical analysis where several members with different mesh sizes are attached to one element. In this study, SPH particles were used to construct a fluid, and finite elements were used to construct a structure. The SPH particles were designated as a slave part and finite element as a master part using the node-to-surface contact algorithm (Hallquist, 2006).

As shown in Fig. 2(a), a node n_s of slave part which is located above the surface of finite element search the nearest master surface and the node m_s. The vector $\mathbf{g}$ is projected onto the master surface which is denoted by the vector $\mathbf{s}$ beginning at m_s and ending at $n_{s'}$. The vectors $\mathbf{c}_i$ and $\mathbf{c}_{i+1}$ are along the edges of the segment S_1 and point to the node on the master surface. The unit normal vector of the master segment is expressed as

$$\mathbf{m} = \frac{\mathbf{c}_i \times \mathbf{c}_{i+1}}{|\mathbf{c}_i \times \mathbf{c}_{i+1}|}, \tag{21}$$

and the projection vector $\mathbf{s}$ is given by

$$\mathbf{s} = \mathbf{g} - (\mathbf{g}\cdot\mathbf{m})\mathbf{m}. \tag{22}$$

A node n_s lies on the segment S_1 where the master element node m_s is located if the following conditions are satisfied (Hallquist, 2006)

$$(\mathbf{c}_i \times \mathbf{s})\cdot(\mathbf{c}_i \times \mathbf{c}_{i+1}) > 0, \tag{23}$$

$$(\mathbf{c}_i \times \mathbf{s})\cdot(\mathbf{s} \times \mathbf{c}_{i+1}) > 0. \tag{24}$$

If n_s lies on or near the intersection of two master segments, Eqs. (23) and (24) are not satisfied, and therefore, the following expression with the use of the maximum value can be applied to searching algorithm (Hallquist, 2006).

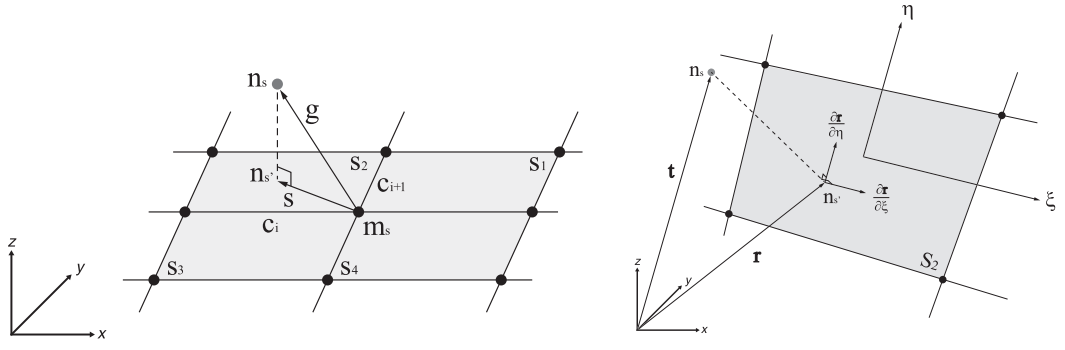

Fig. 2. Schematic diagram of contact searching: (a) Projection of the vector g onto master segment S_1. (b) Location of contact point (Hallquist, 2006; Lee et al., 2016).

$$\frac{\mathbf{g}\cdot\mathbf{c}_i}{|\mathbf{c}_i|}, i = 1, 2, 3, 4, \cdots, \tag{25}$$

where i represent the number of intersection of master segments. After searching the master segment, the coordinate of the contact point $n_{s'}$ on the master segment must satisfy

$$\frac{\partial \mathbf{r}}{\partial \xi}(\xi_c, \eta_c)\cdot[\mathbf{t} - \mathbf{r}(\xi_c, \eta_c)] = 0, \tag{26}$$

$$\frac{\partial \mathbf{r}}{\partial \eta}(\xi_c, \eta_c)\cdot[\mathbf{t} - \mathbf{r}(\xi_c, \eta_c)] = 0. \tag{27}$$

For the hexahedral element as shown in Fig. 2(b), there is no analytical solution for Eqs. (26) and (27). To solve numerically, three iterations using a least-squares projection are used to generate an initial guess, then the equations can be solved using Newton-Raphson iteration.

$$[\mathbf{H}]\begin{Bmatrix}\Delta\xi \\ \Delta\eta\end{Bmatrix} = -\begin{Bmatrix}\mathbf{r}_{,\xi} \\ \mathbf{r}_{,\eta}\end{Bmatrix}\{\mathbf{r}(\xi_c, \eta_c) - \mathbf{t}\}, \tag{28}$$

$$[\mathbf{H}] = \begin{Bmatrix}\mathbf{r}_{,\xi} \\ \mathbf{r}_{,\eta}\end{Bmatrix}\begin{bmatrix}\mathbf{r}_{,\xi} & \mathbf{r}_{,\eta}\end{bmatrix} + \begin{bmatrix}0 & \mathbf{r}\cdot\mathbf{r}_{,\xi\eta} \\ \mathbf{r}\cdot\mathbf{r}_{,\xi\eta} & 0\end{bmatrix}, \tag{29}$$

$$\xi_{i+1} = \xi_i + \Delta\xi, \eta_{i+1} = \eta_i + \Delta\eta. \tag{30}$$

Further details regarding the contact searching and iteration method are described in Hallquist (2006).

3.2. Penalty-based contact

When the slave node n_s pass through the master segment, a reactive force proportional to the penetration depth l is utilized using the penalty-based contact algorithm that gives to prevent the penetration phenomenon and forming a contact interface between the structure and the particle. In this process, the contact force, which is the reaction force of the structure on the particles, can be used to indirectly calculate the fluid force applied by the particles to the structure. The penetration occurs in the following condition.

$$l = \mathbf{n}_i\cdot[\mathbf{t} - \mathbf{r}(\xi_c, \eta_c)] < 0 \tag{31}$$

The reaction force vector $\mathbf{f_s}$ is given by (Hallquist, 2006)

$$\mathbf{f_s} = -lk_{cs}\mathbf{n}_i, \tag{32}$$

where $\mathbf{n}$ is the unit normal vector of the master segment at the contact point, and l is the penetration depth. The contact stiffness for segment-based penalty formulation is given as (Hallquist, 2006)

$$k_{cs}(t) = 0.5\cdot SLSFAC\cdot\begin{Bmatrix}SFS \\ or \\ SFM\end{Bmatrix}\left(\frac{m_1 m_2}{m_1 + m_2}\right)\left(\frac{1}{\Delta t_c(t)}\right)^2, \tag{33}$$

where *SLSFAC* is scale factor for sliding interface penalties with the default value of 0.1. *SFS* and *SFM* are scale factors of the slave and master penalty stiffness, respectively, using a default value of 1. m_1 is the nodal mass of a smoothed particle, and m_2 is the segment mass of the finite element. $\Delta t_c(t)$ is set to the initial solution time step which is updated to prevent unstable behavior (Hallquist, 2006; Lee et al., 2016).

4. Numerical verification

We perform a parametric study to find the optimized parameters for the SPH simulation by using a finite element simulation package LS-DYNA. Through the comparison with analytical results and experiment, the fluid forces exerted on a structure are evaluated, and the important factors are investigated. Numerical simulations are carried out using workstations equipped with dual Intel Xeon E5-2687W (3.4 GHz) CPUs and 128 GB memory.

4.1. Hydrostatic water column on an elastic plate

Existing studies using SPH have shown that both the fluid and the structure are composed of SPH particles, and the maximum fluid force is often overestimated (Silvester and Cleary, 2006; Barreiro et al., 2013). Therefore, in this study, we calculate the maximum hydraulic force more accurately by using the contact force. For the interaction of SPH particles and the solid plate consisting of the finite elements in Fig. 3, the node-to-surface contact condition is imposed between the particles and finite elements (Hallquist, 2006, 2007). The node-to-surface contact algorithm gives a reaction force proportional to the depth of the slave part on the surface of the master part, and therefore, the applied forces by all the water particles on the surface of the structure are calculated by summing up the forces on the structure's surface by each water particle.

The hydrostatic water column on an elastic plate simulation which is originally proposed by Fourey et al. (2017) and utilized by Li et al. (2015) and Khayyer et al. (2018a) is one of the famous benchmark tests to validate the numerical fluid-structure interaction model. Recently, to verify the performance of the FSI solver, Khayyer et al. (2018b) applied the present benchmark test to the coupling simulation of a fluid discretized by Lagrangian particles including ISPH and MPS and a structure modeled as Hamiltonian MPS and SPH particles. In order to verify the interaction of fluid and the elastic plate, we conducted the benchmark test in which a fluid with the dimensions of 1 m × 2 m subjects to the aluminum plate with dimensions of 1 m in length and 0.05 m in height. The water and aluminum plate are modeled with the same as of the schematic diagram as shown in Fig. 3-(a), and the hydrostatic pressure is exerted to the plate due to the gravitational acceleration of the water. The nodes constituting both ends of the aluminum plate are fixed in all directions, and the boundaries of the fluid not contacting with the solid plate are set as symmetric boundaries to make the fluid particles stay within the boundaries. For the numerical model, hexahedral solid elements are used for the elastic material, and the element sizes are 0.025 m in x-direction and 0.0125 m in y-direction, respectively. The water is discretized by smoothed particles with the initial spacing of 0.02 m. The material properties of the numerical model are listed in Table 2.

4.1.1. Effect of smoothing length

The SPH method expresses the fluid field with a number of volumetric particles, and the accuracy of the simulation result is affected by the number of SPH particles constituting the fluid as well as the interaction range. The number of particles included in the calculation can be conveniently changed by changing the initial spacing of the particles, and the interaction range is manipulated by adjusting the size of the calculation range, the so-called smoothing length.

The smoothing length determines the range of computation with other particles and therefore has a considerable effect on the accuracy of the analysis results and on the computational efficiency. The constant smoothing length parameter λ is multiplied by the initial particle spacing d to compute the actual smoothing length

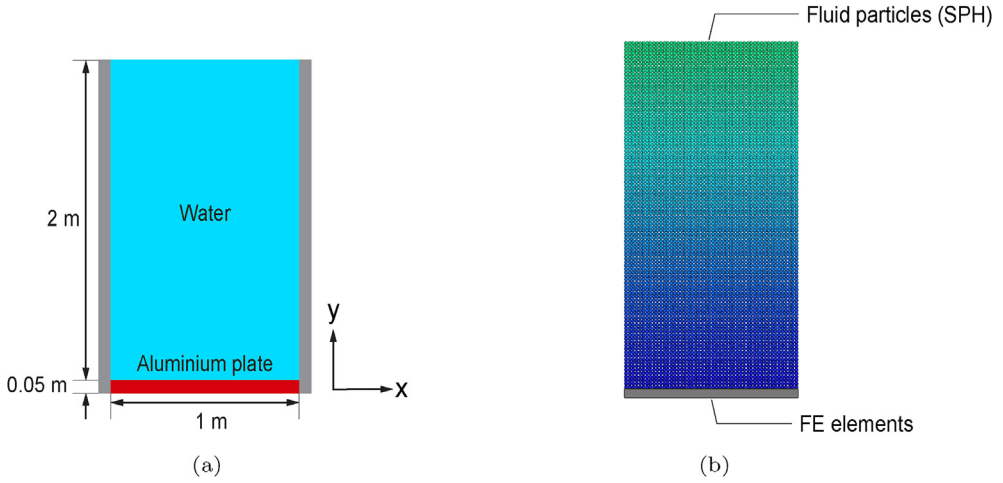

Fig. 3. Hydrostatic water column on an elastic plate: (a) Schematic (Khayyer et al., 2018a; Fourey et al., 2017), (b) Numerical model.

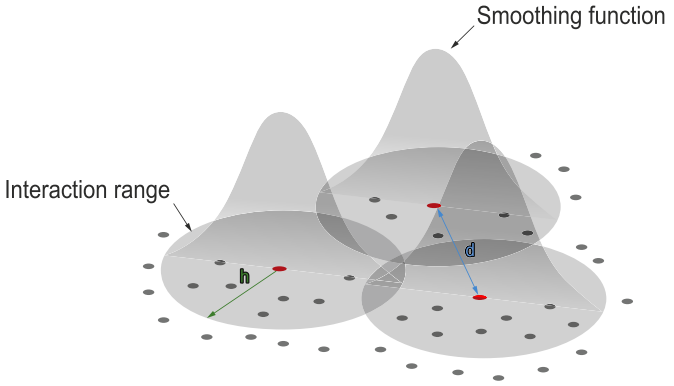

Fig. 4. Smoothing length and particle spacing in SPH simulation.

Table 1
Gruneisen coefficients (Boyd et al., 2000).

C (m/s)	S_1	S_2	S_3	E (J/kg)	γ_0	a	ρ_0 (kg/m^3)
1484	1.979	0	0	3.072×10^5	0.11	3	1000

Table 2
Properties of fluid and solid materials (Khayyer et al., 2018a; Fourey et al., 2017).

Material properties	Water	Aluminum
Mass density (kg/m^3)	1000	2700
Dynamic viscosity (Pa•s)	0.0015	–
Young's modulus (GPa)	–	67.5
Poisson's ratio, ν	–	0.34

$h(t)$ (Fig. 4), then the range in which the particles influence each other is written as

$$h(t) = d \cdot \lambda. \tag{34}$$

The smoothing length parameter λ within the range from 1.05 to 1.3 has been widely used for the analysis (Hallquist, 2007). The value cannot be smaller than 1, but the calculation time increases if the value is larger than 1.3. For the fast calculation, it is not recommended to use larger value of the smoothing length parameter λ (Hallquist, 2006).

The smoothing length factors λ are set to be 1.05, 1.2, and 1.3, and the time history of the deflection at the central point of an aluminum plate is shown in Fig. 5(a). According to the analytical solution, the deflection at the central point of the aluminum plate is −6.85E-05 m (Khayyer et al., 2018a; Fourey et al., 2017). Compared with the analytical result, the accuracy of numerical results increases by reducing λ, and models with the length λ of smaller than 1.2 show good agreements, compared to the theoretical formulas (Fig. 5(a)). However, in the case $\lambda = 1.3$, the initial oscillation due to the gravitational acceleration is not stabilized until 0.5 s, and the amplitude of the initial oscillation increases by increasing the length λ in the simulation.

Fig. 5(b) shows the time history of the hydrodynamic pressure at the central point of an aluminum plate. In the case $\lambda = 1.05$ and 1.2, the deflection of the plate and hydrostatic pressure converges to −6.85E-05 m and 19.6 kPa respectively, as the smoothed particles reach to the equilibrium state after the significant number of iterations. Due to the gravitational acceleration, the time series of the deflection and pressure fluctuates, and the amplitude of the initial oscillation and time for stabilization increases by increasing the length of λ. This could be due to the boundary effect of the particles by the length of λ. In general, the larger the interaction range, the more particles are used to calculate the governing equation causing the improvement of the accuracy. However, if the smoothing length is greater than a certain value, more particles are contained in the interaction range resulting in poor results. Since the computation time tends to increase as the smoothing length λ increases, the value between 1.05 and 1.2 could be used for effective calculation of hydrostatic problem. Overall, it is possible to accurately calculate the hydrostatic pressure and fluid-structure interaction by using the contact algorithm in the SPH simulations.

4.1.2. *Effect of calculation time step*

In the numerical simulation, the time step size roughly corresponds to the transient time of an acoustic wave through an element using the shortest characteristic distance (Hallquist, 2007). The calculation time steps for finite element and smoothed particles are determined based on the CFL condition, and the constant time step scale factor β is multiplied to the minimum time step for stable calculation. Therefore, the new time step is given by

$$\Delta t^{n+1} = \beta \times min\{\Delta t_1, \Delta t_2, \cdots, \Delta t_N\}, \tag{35}$$

where N is the number of elements, $\Delta t_1, \Delta t_2, \cdots, \Delta t_N$ represent the

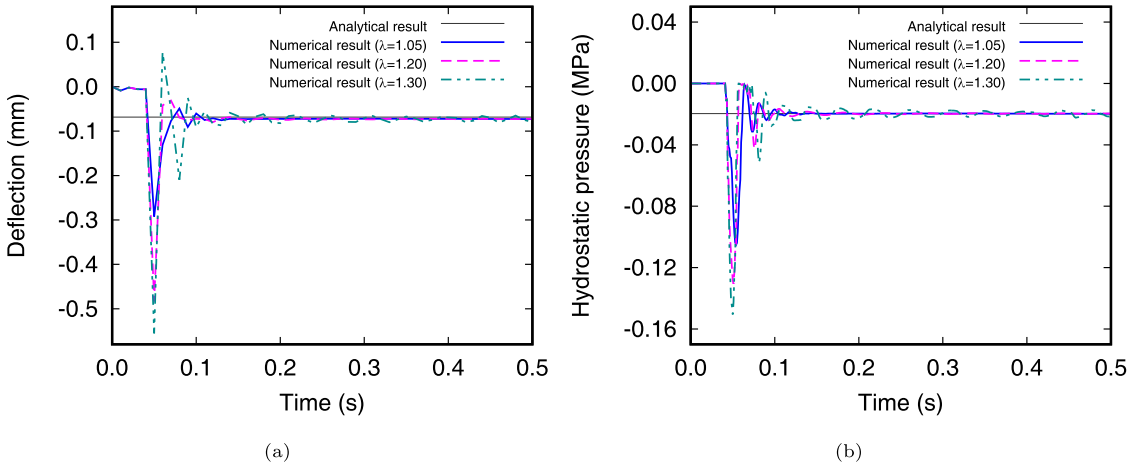

Fig. 5. Time history of the deflection and hydrostatic pressure at the central point of an aluminum plate under the water column.

time step calculated for SPH and FEM, and the scale factor β is set to a default value of 0.9. It is not recommended to use the time step scale factor β greater than 0.9 for stable calculation (Hallquist, 2007). Using the same model of Section 4.1.1, the numerical analysis is performed by varying the time step factor β.

The smoothing length λ is fixed as 1.2, and the time step scale factor β is set to be 0.9, 0.8, and 0.7, respectively. The deflections and hydrodynamic pressures are shown in Fig. 6. Due to the gravitational acceleration, the deflection and pressure profiles fluctuate before 0.2 s and stabilize after 0.3 s. Compared with the analytical results, the numerical deflection and hydrostatic pressure results show good agreement regardless of the factor β. In the present simulation, the critical length is calculated by selecting the shortest characteristic distance between the particle spacing of the SPH element and the element size of solid, and the time step is calculated by dividing the critical length by the wave velocity determined by the material properties. This process is repeated at every step of the calculation, and β less than 1 is additionally multiplied to the time step. Even if the maximum value of β (0.9) is applied to time step, a stable time step can be utilized, and therefore, the coupling between SPH and FEM can be effectively simulated in analyzing fluid-structure interaction. However, since the total computation time increases with decreasing β, it is advantageous to use 0.9 for efficient calculation.

4.2. Dam-break simulation

Dam-break experiment was carried out by Yeh, Petroff, and Arnason at the University of Washington (Gómez-Gesteira and Dalrymple, 2004; Gómez-Gesteira et al., 2012; Arnason, 2005), in which the impacting force by water on a structure was measured after suddenly removing the gate in a tank as shown in Fig. 7(a). The experiment was carried out using a rectangular shape water tank of 1.6 m in length, 0.61 m in width and 0.75 m in depth. The water with dimensions 0.4 m long, 0.61 m wide and 0.3 m high was located at the left side of the water tank. An acrylic structure with a square cross-section of 0.12 m by 0.12 m and 0.75 m high is located in the water tank. The bottom section from the gate to the right end of the water tank is called a bed. In the experiment performed by Yeh and Petroff, a complete drainage of the bed was difficult so that the depth of the bed was maintained to be 0.01 m (Gómez-Gesteira and Dalrymple, 2004; Gómez-Gesteira, 2013). Further details of the experiment are described in Arnason (2005). The force was measured with a load cell, and velocities of fluid were recorded. As shown in Fig. 7(b), the numerical results have been compared with these experiment data by several researchers. However, the wave forces often have been overestimated (Silvester and Cleary, 2006; Barreiro et al., 2013).

In order to find the optimized parameters to ensure accurate

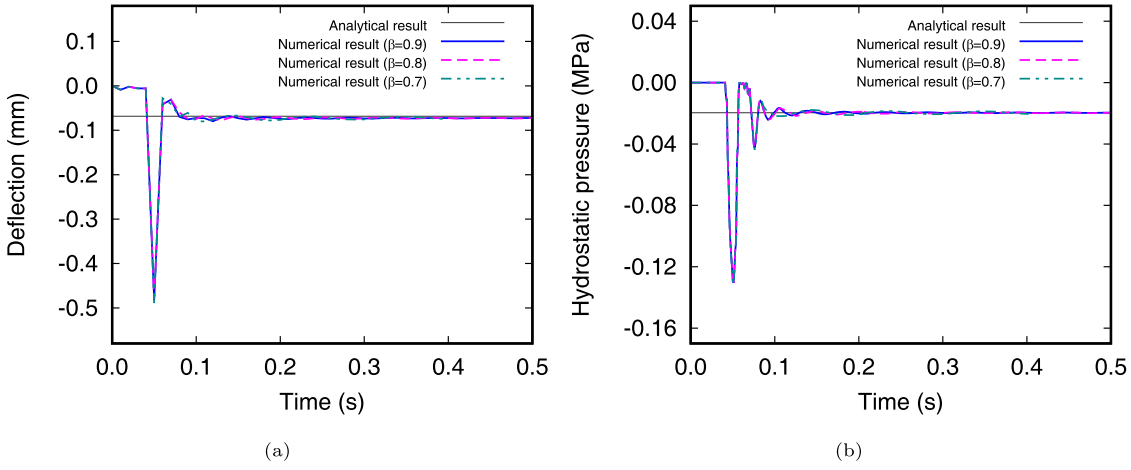

Fig. 6. Time history of the deflection and hydrostatic pressure at the central point of an aluminum plate corresponding to scale factor β.

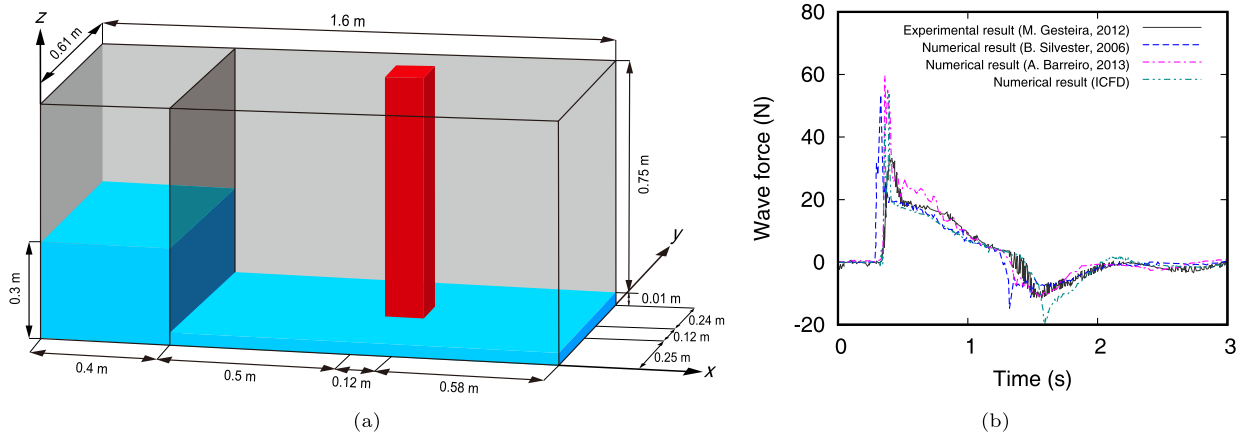

Fig. 7. Schematic diagram of dam-break experiment and comparison of wave forces (Gómez-Gesteira et al., 2012; Gómez-Gesteira, 2013; Silvester and Cleary, 2006; Barreiro et al., 2013).

calculation, we conduct a parametric study and compare the results with the experiment results. The numerical model is made with the same dimensions as of the experiment configuration (Fig. 7(a)), and the water pile sinks and breaks by the gravitational force as soon as the analysis starts.

As shown in Fig. 8, the solid column structure is discretized with 162 8-node solid finite elements, and dimensions of each element are 40 mm × 40 mm × 40 mm. The water tank and water are modeled by SPH particles with initial particle spacing of 5 mm, 7.5 mm, and 10 mm. The size of the elements is much larger than the initial spacing of the SPH particles, which is convenient to collect all the forces acting on the finite element surfaces. In this simulation, to simulate the boundary walls, two layers of SPH particles are arranged and constrained in the *x*-, *y*-, and *z*-directions. Also, the finite element nodes that compose the bottom side of the column structure are fixed in motion in all directions. In the experiment, an aluminum rod was used to fix the upper part of the structure (Arnason, 2005). In all the simulation of the present study, it was assumed that there are no movements because the displacement of the upper part of the structure is less than 1 μm. The SPH particles are modeled using a water material while the finite elements consisting the column are modeled by using an elastic material. The material properties are listed in Table 3.

Since the equation of state affects the isotropic pressure of the fluid particle, the pressure of the wave acting on the column changes according to the selection of the equations of state.

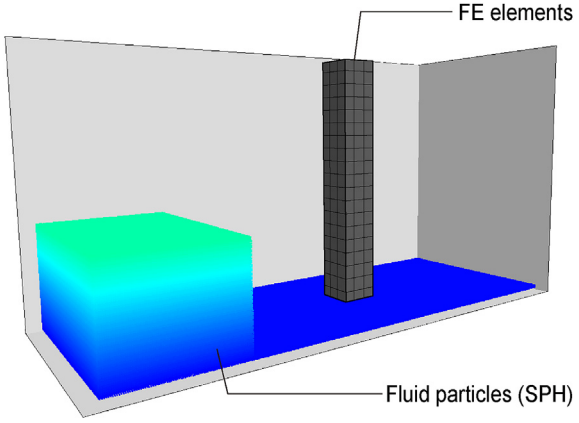

Fig. 8. SPH model of fluid and finite element model of solid.

Table 3
Properties of fluid and solid materials (Acrylic, 2013).

Material properties	Water	Acrylic
Mass density (kg/m^3)	1000	1190
Dynamic viscosity (Pa•s)	0.0015	–
Young's modulus (GPa)	–	3.1
Poisson's ratio, ν	–	0.35

Numerical simulation results in literature commonly exhibit the overestimation of the peak wave force although the overall wave force profiles agree with the experiment results. Therefore, instead of using the Tait EOS which has been widely used in literature, the Gruneisen EOS (Eq. (15)) is employed in this study.

4.2.1. Effect of initial particle spacing and time step

In order to find the optimal conditions for simulating the dam break phenomenon, the numerical simulations are carried out with different initial particle spacing and different smoothing lengths, respectively. Firstly, the smoothing length factor λ and time step scale factor β are fixed to the default value, and the initial particle spacing, which constitutes the fluid and boundary walls, is decreased from 10 mm to 5 mm by 2.5 mm. The simulation parameters are summarized in Table 4.

In the simulation of Cases A1, A2, and A3, only the initial spacing of the particles constituting the fluid and boundary wall has been changed. With the removal of the gate, the gravity force causes the change of the arrangement of the particles constituting the fluid, and water starts flowing to the right direction and interacts with the solid column structure and the right side of the water tank as shown in Fig. 9.

After the wave collides with the column, the water flows around the column at $t = 0.5$ s, and the height of the water surface becomes maximum as shown in Fig. 9(b). The fluid meets the wall on the right side of the water tank, yielding the maximum water level of the right end of the tank at $t = 1.1$ s (Fig. 9(e)). Then, the wave is reflected in the opposite direction and return toward the column. Approximately from time $t = 2.0$ s, the wave starts to form an equilibrium state. A comparison of the stress field in the structure is shown in Figs. 9(c) and (f). At $t = 0.5$ s, the von Mises stress in the surface of the structure is concentrated at the area exerted by the breaking wave. On the other hand, in the case of $t = 1.1$ s, the maximum stress is calculated along the *z*-coordinate of the same location as the water level. The maximum von Mises stresses measured at the front side of the column elements are 9.6 kPa

Table 4
Initial spacing and numbers of particles.

Case No.	Initial particle spacing	Number of particles
A1	10.0 mm	172,236
A2	7.5 mm	348,162
A3	5.0 mm	940,856

Table 5
Error of wave force between experiment data and numerical results for Regions I, II, and III.

Case	A1	A2	A3
Initial particle spacing	10.0 mm	7.5 mm	5.0 mm
ER /ER_{A3} (I + II + III)	1.586	1.231	1.0
ER /ER_{A3} (I)	1.478	0.961	1.0
ER /ER_{A3} (II)	1.666	1.395	1.0
ER /ER_{A3} (III)	1.293	0.883	1.0
ER /ER_{A3} (I + II)	1.594	1.242	1.0

($t = 0.5$ s) and 8 kPa ($t = 1.1$ s), respectively, and the value is larger when the breaking waves directly acting on the column.

When a dam-break wave acts on a fixed solid structure, the hydrodynamic pressure of the nearly incompressible fluid can be estimated by using the relation between the pressure and the velocity squared. The stress field of the structure is also calculated through the velocity changes of the fluid particles contacting with the structure. The x-directional velocity of the dam-break wave is shown in Fig. 10. At $t = 0.2$ s, the maximum velocity is calculated at the bottom side of the water column which is collapsed by the gravitational acceleration, and the dam-break wave acts on the column at $t = 0.5$ s. Fig. 10(b) shows that the velocity of the fluid particles in contact with the structure converges to zero, indicating that all the kinetic energy of the fluid is converted to dynamic pressure in the structure. Therefore, the difference in the value of the von Mises stress shown in Figs. 9(c) and (f) can be explained by the difference in magnitude of hydrodynamic pressure.

The resultant forces acting on the rectangular column are calculated by summing up all the forces by SPH particles on the surfaces of finite elements and are shown in Fig. 11. In order to investigate the calculated wave forces more precisely, the time domains are divided into three regions: Region I from $t = 0$ s–1.0 s, Region II from $t = 1.0$ s–2.0 s, and Region III from $t = 2.0$ s–3.0 s. In Region I, the maximum positive wave force occurs due to the sudden flow of the water and collision onto the column; in Region II, the negative force is observed due to the wave coming back, reflected on the right side of the water tank. In Region III, wave force decreases to zero.

The errors of the numerical results with respect to the experiment result are normalized to the error of Case A3, as summarized in Table 5. Overall, the error of Case A3 is smaller than others, but in specific regions, the error of other cases might be smaller than the value of Case A3. For example, in Region I, Case A2 yields a smaller error than Case A3. The arrival time of the Case A3 is faster than the experiment results, and the larger the initial particle spacing, the slower the fluid velocity is. However, the peak force of Case A3 is closer to the experiment result as shown in Fig. 11. Therefore, the maximum force of Case A1 and Case A2 is greater than the experimental results, and this implies that the more particles located in the calculation range, the more accurate force can be obtained. The normalized error of Case A1 and Case A2 in Region II is much larger than that of Case A3, reduction of calculation range is needed to improve the error in Region II while keeping the initial particle spacing to 5 mm.

By reducing the distance of SPH particles, the number of particles increases exponentially by order of 3 in the three-dimensional domain, which accompanies the significant increase in the computational cost and calculation wall-clock time as shown in Fig. 12 although the error of the simulation decreases linearly. For

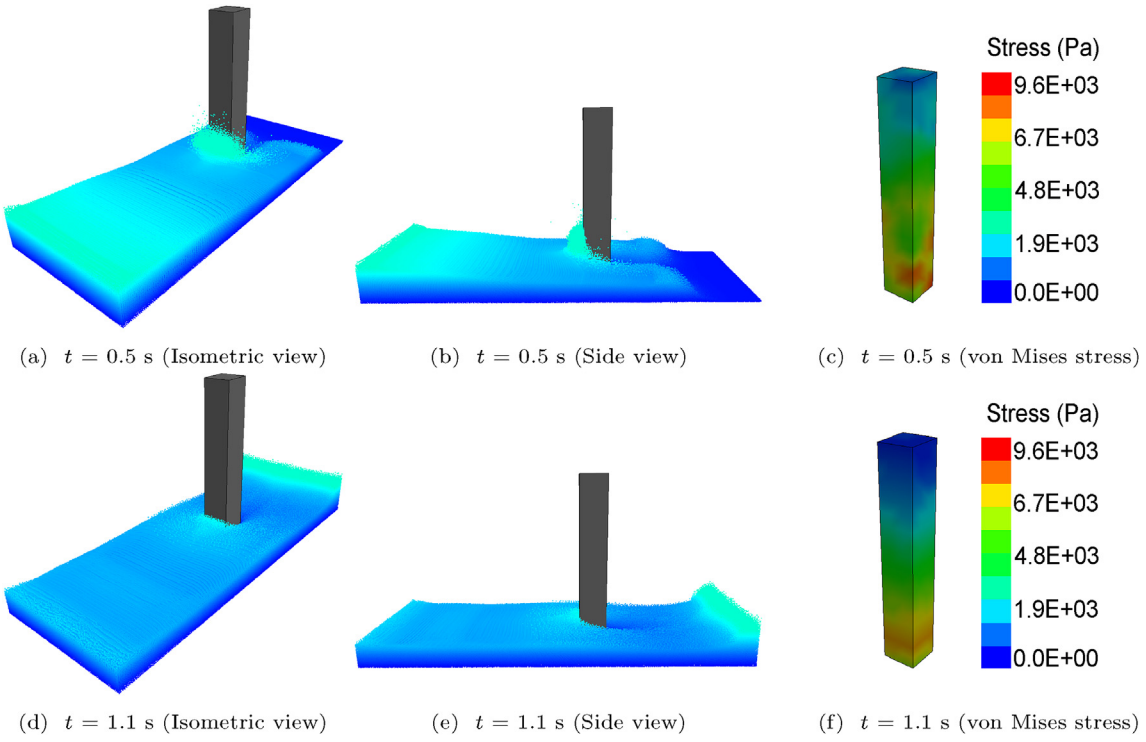

(a) $t = 0.5$ s (Isometric view) (b) $t = 0.5$ s (Side view) (c) $t = 0.5$ s (von Mises stress)

(d) $t = 1.1$ s (Isometric view) (e) $t = 1.1$ s (Side view) (f) $t = 1.1$ s (von Mises stress)

Fig. 9. Free surface wave interaction with a rectangular column with the parameters of Case A2.

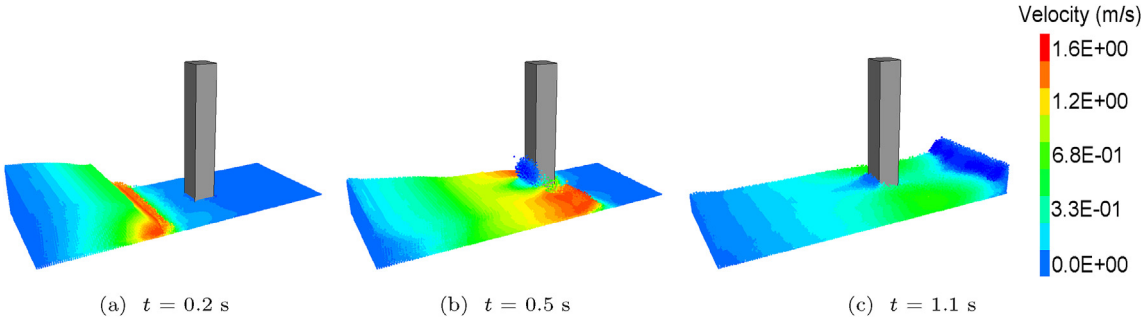

Fig. 10. Horizontal velocity field of the smoothed particles.

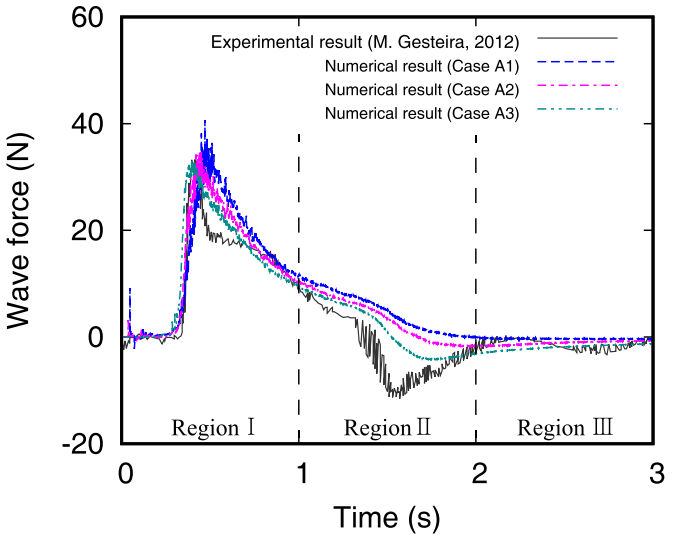

Fig. 11. Comparison of wave forces by experiment (Gómez-Gesteira et al., 2012) and numerical simulations.

example, in Case A1, with the particle spacing of 10 mm, the calculation time is 50 h, but in Cases A2 and A3, the times increase to 80 h and to 200 h, respectively. In order to confirm the improvement of the numerical result by varying the time step scale factor, $\beta = 0.8$ is employed in the model with the same particle interval as Case A3. As in the hydrostatic pressure calculations in Section 4.1, the hydrodynamic force in dam-break problem does not effectively change by varying the time step scale factor. Compared with the experimental results, the difference in normalized error is 0.9%, but the wall-clock times increase by 25%–250 h. With the use of $\beta = 0.9$, a stable time step can be determined and the smallest total computation time is utilized. For the computationally efficient use of the SPH method, the trade-off by increasing the number of particles needs to be considered in determining the initial spacing of SPH particles while ensuring enough accuracy using the available computational resources.

4.2.2. *Effect of smoothing length*

To investigate the effect of the smoothing length and to find the optimal value, we perform analyses changing the smoothing length parameter λ from 1.05 to 1.30 by 0.05, as summarized in Table 6 while keeping the particle spacing as 5 mm.

As the length parameter decreases from 1.3 to 1.05, the wave height increases when the SPH water particles contact with SPH particles constituting the solid wall of the water tank on the right side as shown in Fig. 13. At $t = 0.5$s, the maximum von Mises stress is uniformly calculated at the front side of the structure due to the dam-break wave, and the increment of the dam-break wave height is most noted in Case B1 at $t = 1.1$s.

As shown in Fig. 14(a), in Region I, the larger the parameter λ, the slower the peak arrival time is. As in Section 4.2.1, the magnitude of the numerical force also tends to decrease with increasing calculation range, and the negative wave force approximately at $t = 1.6$ s by the reflected wave decreases in the magnitude with increasing λ. These results can be explained by the fluid velocity. In Region I, the

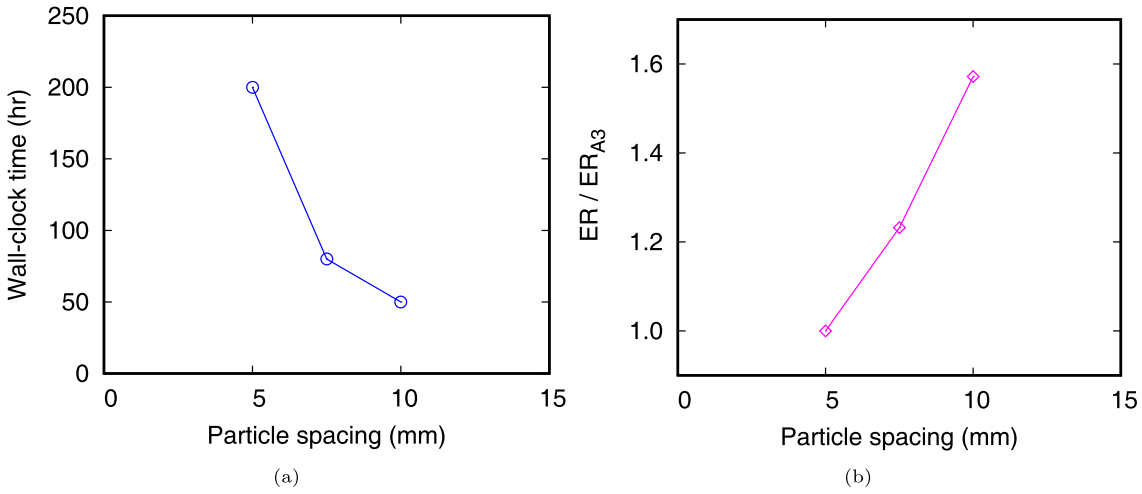

Fig. 12. Wall-clock time and normalized error according to the particle spacing.

Table 6
Smoothing lengths.

Case No.	B1	B2	B3	B4	B5	B6
Smoothing length parameter (λ)	1.05	1.10	1.15	1.20	1.25	1.30

greater the number of particles included in the calculation range, the slower the arrival time is. The lower the maximum force is because the fluid velocity is also smaller. In Region II, the negative pressure due to the reflected wave can be also described by the fluid velocity. As described in Section 4.2.1, the hydrodynamic force is mainly determined by the fluid velocity, and the velocity decreases as the length λ increase regardless of the region. Therefore, the length λ and fluid velocities are inversely correlated.

The errors between the experiment data and numerical simulations are normalized to the error calculated in Case B4 as summarized in Table 7. Overall, the error increases if the factor λ is smaller than 1.1 or larger than 1.2 as shown in Fig. 14(b). However, the error in each region shows a different correlation pattern with the change of the factor λ as shown in Fig. 14(c). It should be noted that the error in Region II is proportional to the parameter λ, but errors in Regions I and II are inversely proportional to the parameter.

Fig. 15shows the wave forces calculated with different parameters λ and the numerical simulation results in the literature. In Region I, the dam-break wave of Case B2 arrives at the column faster than that of the Case B4, and the wave force of Case B2 is slightly greater than that of Case B4. In Region II, the force in Case B2 is closer to the experiment data than the force of Case B4. In order to satisfy both the maximum force and the fluidity in the hydrodynamic problem, a proper fluid velocity is required, and the relationship between smoothing length and fluid velocity can be used to derive appropriate results.

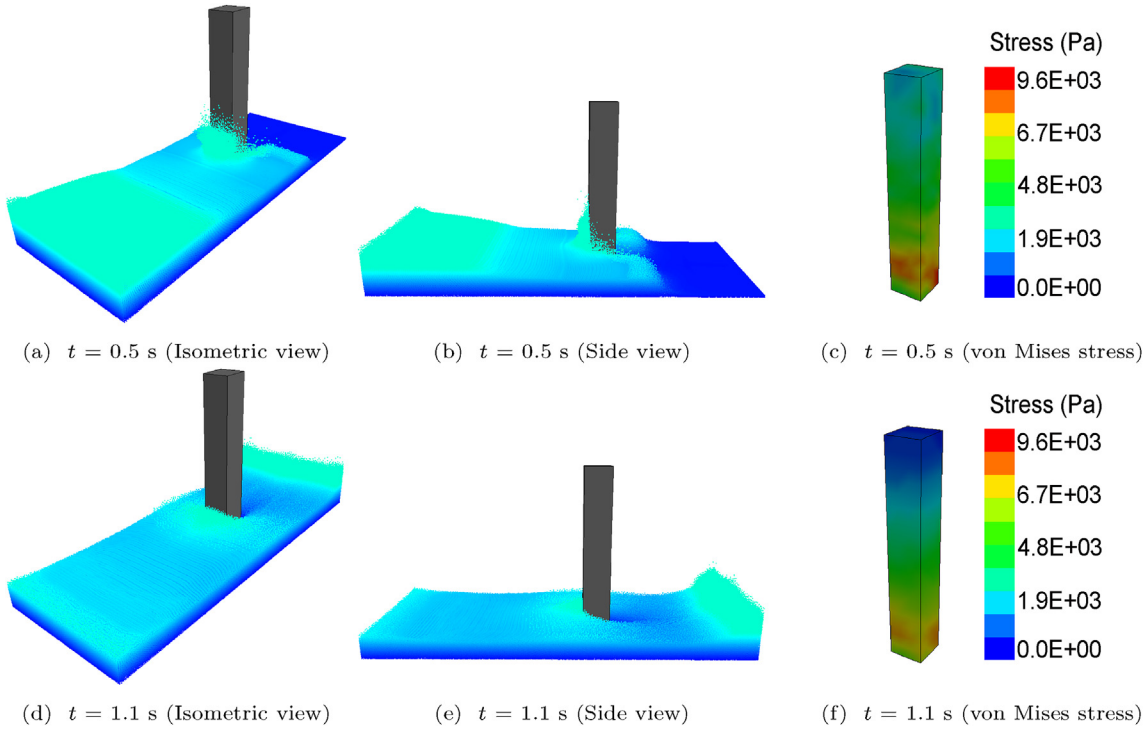

Fig. 13. Free surface wave interaction with a rectangular column with the parameters of Case B1.

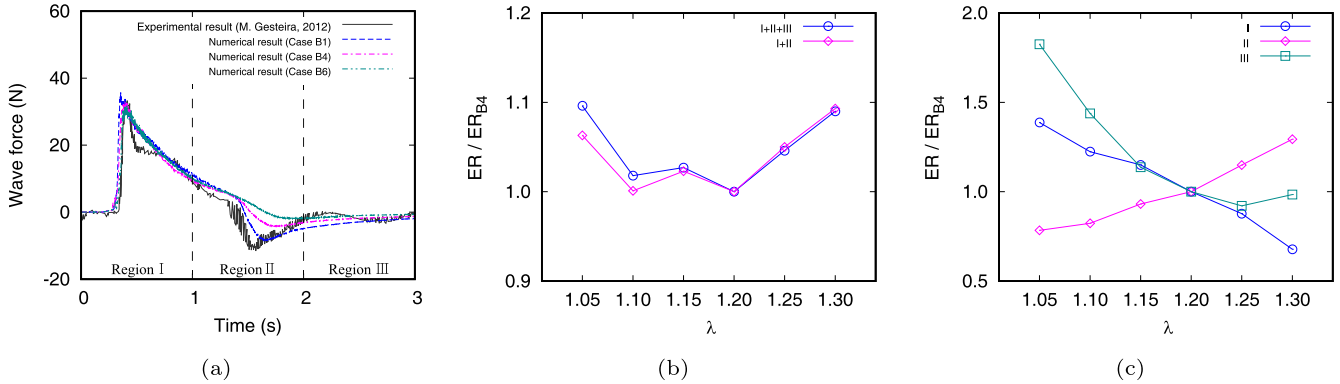

Fig. 14. (a) Comparison of wave forces by experiment (Gómez-Gesteira et al., 2012) and numerical simulations. (b) and (c) Normalized errors according to the change of the influence range factor λ.

Table 7
Error of wave force between experiment data and numerical results for Regions I, II, and III.

Case	B1	B2	B3	B4	B5	B6
Smoothing length (λ)	1.05	1.10	1.15	1.20	1.25	1.30
ER /ER$_{A3}$ (I + II + III)	1.096	1.018	1.027	1.000	1.046	1.090
ER /ER$_{A3}$ (I)	1.387	1.224	1.150	1.000	0.877	0.678
ER /ER$_{A3}$ (II)	0.784	0.823	0.931	1.000	1.149	1.294
ER /ER$_{A3}$ (III)	1.825	1.438	1.137	1.000	0.921	0.984
ER /ER$_{A3}$ (I + II)	1.063	1.000	1.023	1.000	1.050	1.093

Using the Gruneisen equation of state and coupling with FEM elements, it is shown that the maximum wave force is more precisely calculated than the results in the literature (Silvester and Cleary, 2006; Barreiro et al., 2013). As shown in Fig. 15–(a), a difference of results from Cases B4 and B2 is trivial. Therefore, the smaller factor $\lambda = 1.1$ or 1.2 might be chosen to alleviate the computational cost.

5. Application

5.1. Comparison of forces by open surface flow

The current and wave are two major sources to make forces exerted on offshore structures. Fluid forces applied to a structure sitting in the flow consist of drag and inertia forces, and the magnitudes are determined by the profiles of the wave and current as well as the geometries of the structure.

If the diameter D of the offshore cylindrical structure is relatively smaller than the wavelength L, then the change of the wavelength might be ignored. With this approximation, the exerted force by the fluid on a fixed cylindrical column per unit length is expressed by summing up the drag force, hydrodynamic force, and Froude-Krylov force (Sumer and Fredsøe, 2006) as

$$f_x = \frac{1}{2}\rho\, C_D D u|u| + \rho C_m \frac{\pi D^2}{4}\dot{u} + \rho \frac{\pi D^2}{4}\dot{u}, \tag{36}$$

where u and $\dot{u}$ are the horizontal velocity and acceleration, respectively, ρ is the mass density of water, C_D and C_m are the drag and hydrodynamic coefficients, respectively. The Froude-Krylov force expressed in the last term of Eq. (36) is the hydrodynamic force aroused from the gradient of the unsteady pressure field. Hence, the force depends only on the fluid velocity. By defining an inertia coefficient $C_M (= C_m + 1)$, the Morison equation is written as (Morison et al., 1950)

$$f_x = \frac{1}{2}\rho\, C_D D\, u|u| + \rho\, C_M \frac{\pi D^2}{4}\dot{u}, \tag{37}$$

where the first term is the drag force, and the second term is the inertia force. Conventionally, the drag and inertia coefficients, which are experimentally obtained, are expressed as functions of Reynolds number (Re) and Keulegan-Carpenter number (K_C) as in Table 8.

If we consider a circular cylinder moving at the velocity u_s in a flow, the term u in the first and second terms of Eq. 36 might be replaced with $(u - u_s)$, ending up with the modified form of the Morison equation as

$$f_x = \frac{1}{2}\rho\, C_D\, D(u - u_s)|u - u_s| + \rho \frac{\pi D^2}{4} C_m \left(\dot{u} - \dot{u}_s\right) + \rho \frac{\pi D^2}{4}\dot{u}, \tag{38}$$

where u_s and $\dot{u}_s$ are the horizontal velocity and acceleration of the solid structure, respectively. In Eq. (36), the drag force and hydrodynamic-mass force are caused by the pressure effects due to the presence of structures in the streamline. It should be noted that the Froude-Krylov force is associated with absolute acceleration of the fluid. Therefore, it is represented by the acceleration of the fluid alone. The resultant force acting on the fixed vertical cylinder is represented by integrating Eq. (36) as (Chella et al., 2012)

Table 8
Morison coefficients (Clauss et al., 1992).

	$Re \le 10^5$		$Re > 10^5$	
	C_D	C_M	C_D	C_M
$K_C < 10$	1.2	2.0	0.6	2.0
$K_C \ge 10$	1.2	1.5	0.6	1.5

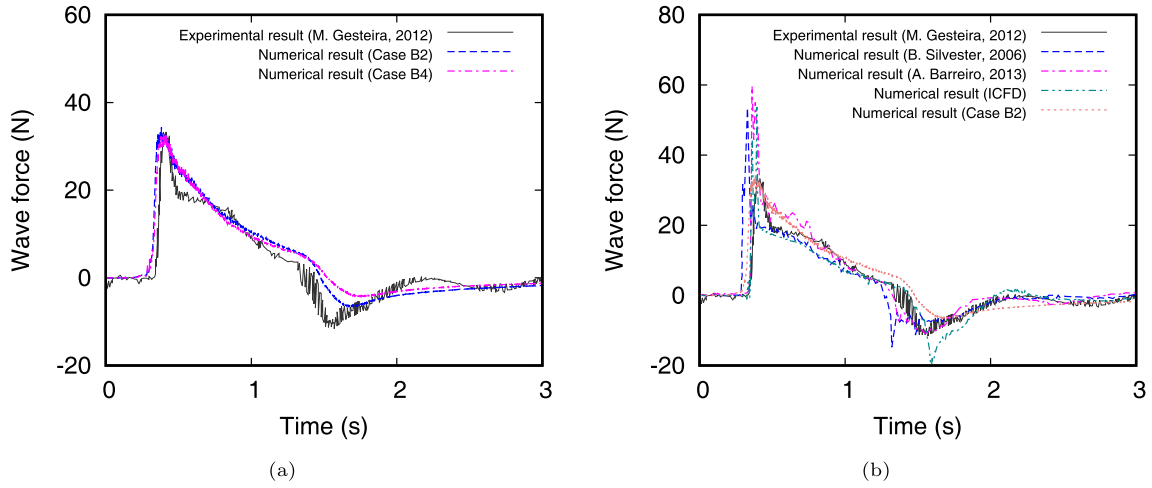

Fig. 15. (a) Numerical results of dam-break simulation and (b) comparison of wave forces.

$$F = \int_{-h}^{\eta} \frac{1}{2}\rho\, C_D D(u-u_s)|u-u_s|dz + \int_{-h}^{\eta} \rho \frac{\pi D^2}{4} C_m(\dot{u}-\dot{u}_s)dz + \int_{-h}^{\eta} \rho \frac{\pi D^2}{4}\dot{u}dz, \tag{39}$$

where h is the average water depth, and η is the free surface elevation on the surface of the cylinder in Fig. 16.

A solid column, which has a height of 0.4 m, an inner diameter of 0.06 m and an outer diameter of 0.12 m, stands vertically in a water tank of dimensions 1.5 m by 0.3 m, of which the water depth is 0.1 m as shown in Fig. 17(a). The column structure is discretized with 156 8-node solid finite elements of the height of 0.03 m, and the inner and outer circumferential lengths are 0.016 m and 0.031 m, respectively. In order to impose the contact interaction of the water and the wall of the water tank, the water and the wall are modeled using the SPH particles of the water material and of the Gruneisen equation of state. On the other hand, the contact between the SPH fluid particles and the solid finite elements is calculated by summing up the particle forces exerted on the outer surfaces of the finite elements (Fig. 17-(b)).

The velocity profile is divided into three regimes as shown in Fig. 18. First, in Section I, the velocity is zero for 0.2 s making the SPH particles constituting the fluid are stabilized by the gravity. In Section II, the velocity gradually increases to 1.4. In Section III, the solid model moves at a constant speed resulting in the constant relative velocity between the solid column and the fluid. As shown in Fig. 19, the SPH fluid particles interact with the solid column moving in the horizontal direction, and the elevation increases as the horizontal speed increases. The maximum rise is observed at $t = 0.6$ s as shown in Fig. 20(a). If the diameter of the offshore structure is smaller than the wavelength of the fluid, the wave force

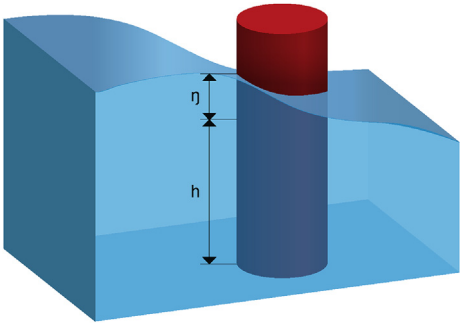

Fig. 16. Cylindrical structure in open surface water. The wave profile is obtained by summing up the average water depth h and the free surface elevation η.

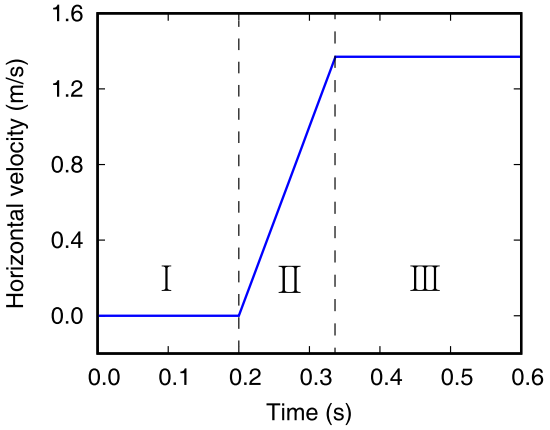

Fig. 18. Horizontal velocity profile of the solid column.

on the moving structure can be analytically calculated using the Morison equation, which includes drag force, hydrodynamic force, and the Froude-Krylov force.

In this example, in order to validate this methodology, the numerical result is compared with the analytical values calculated by using the modified Morison equation in Eq. (39). The elevation height of the fluid on the column surface is obtained by moving the solid column in the horizontal direction, and the acceleration is calculated by differentiating the velocity profile in Fig. 18. The drag coefficient C_D is set to 1.2, and the inertia force coefficient C_M to 2.0 in order to calculate the fluid force on the solid surfaces by using the Morison equation.

Fig. 20(b) shows the analytical results calculated with and without considering the fluid elevation η on the solid column surface as well as the numerical results calculated with the smoothing lengths λ 1.1 and 1.2, respectively. In the numerical simulation, the node-to-surface contact algorithm gives a reaction force proportional to the depth of the slave part on the surface of the master part when the slave and master parts are defined. Therefore, by summing up all reaction forces acting on the surfaces of the finite elements representing the solid column, the surface forces acting on the column is calculated.

For the calculation of the Morison equation considering the elevation η, the height profile of the water surface calculated by the numerical simulation is utilized. This additional consideration yields difference in the analytical results. As shown in Fig. 20(b), the magnitude of the analytically estimated force without incorporating the elevation η is smaller than the value obtained by considering the elevation η. Overall, the numerical result shows good improvement compared with the analytical result that is obtained with consideration of the elevation η.

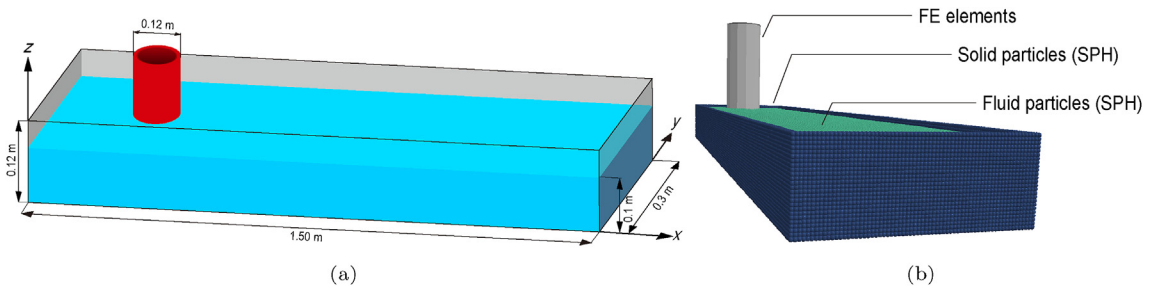

Fig. 17. (a) Configuration and (b) discretization of a moving cylindrical object in the open surface fluid.

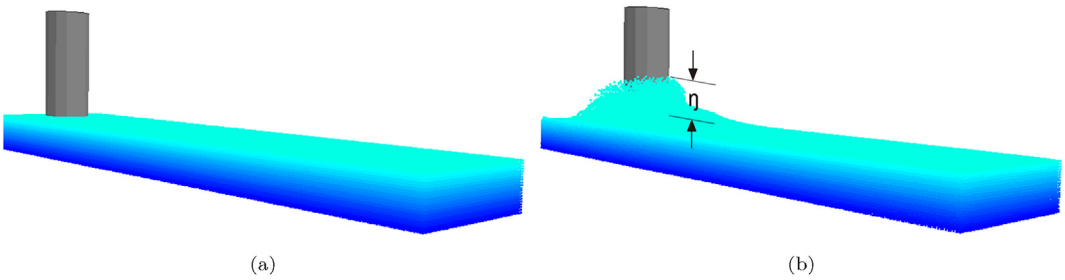

Fig. 19. Cylindrical structure in water.

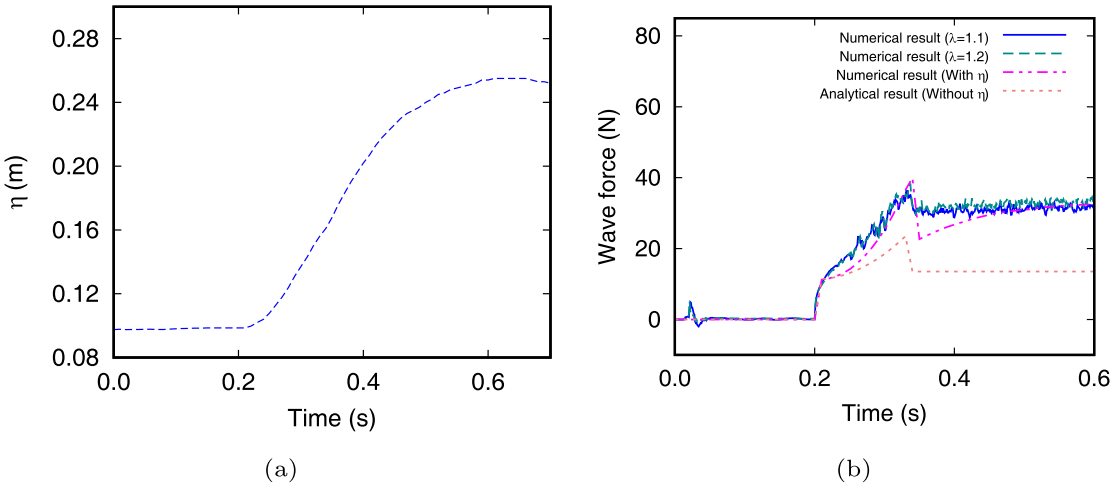

Fig. 20. Analytical and numerical results using Morison equation.

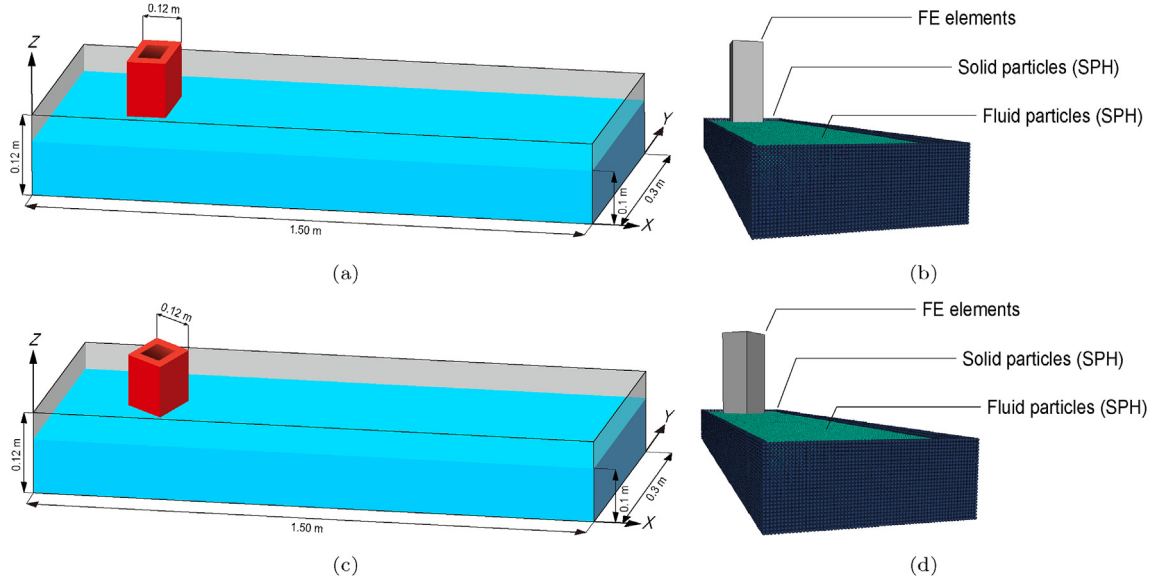

Fig. 21. Configuration and discretization of a moving structure of square and diamond cross-section in the open surface fluid.

5.2. Comparison of forces in the use of various cross sections

In order to confirm that the force by moving solid using various cross-section columns is accurately calculated, we perform the numerical simulations in which a fluid with the dimensions of 1.5 m × 0.3 m × 0.1 m modeled by smoothed particles. As shown in Fig. 21, the column structures with square and diamond cross-section are discretized with hexahedral 8-node solid elements, and the element size is 0.03 m. Both square and diamond cross-section models have a height of 0.4 m, and one side of each cross-section is 0.12 m. An elastic material model is used to represent the acrylic, and the material properties listed in Table 3 are applied

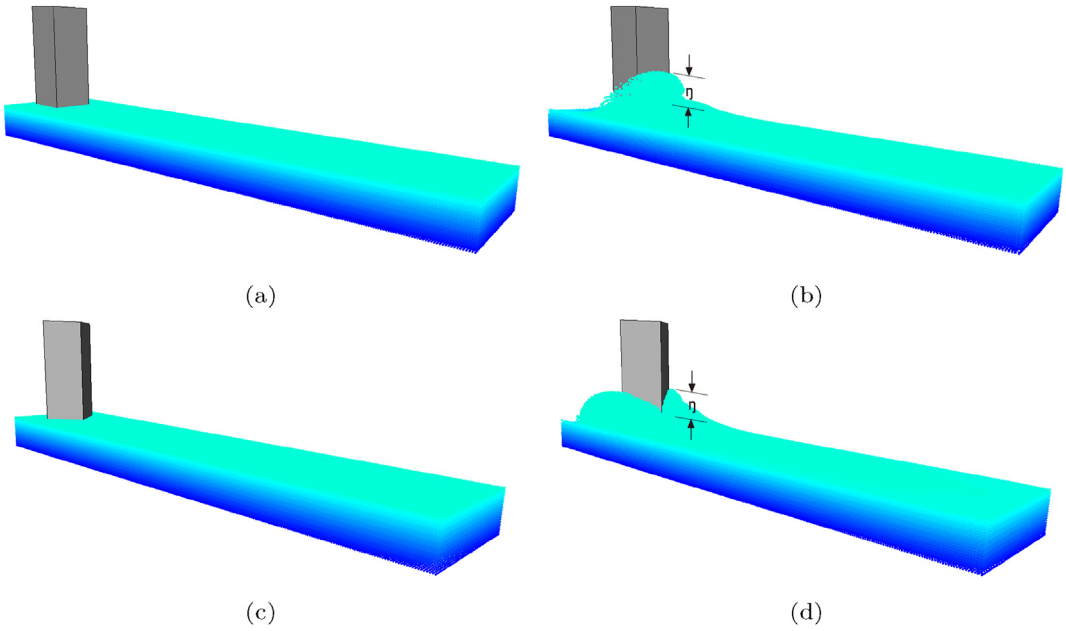

Fig. 22. Moving structures of various cross sections in the fluid.

Table 9
Morison coefficient in accordance with the cross-section (Sumer and Fredsøe, 2006; Sarpkaya, 2010).

Cross-section	C_D	C_M
Square	1.6–1.9	2.186
Diamond	1.5–1.6	2.194

to the water tank and fluid.

The column structure is initially at rest for 0.2 s to stabilize the gravitational acceleration, then accelerates to a maximum velocity of 1.4 m/s as shown in Fig. 18. Due to the horizontal motion of the solid column, the free surface elevation increases as the velocity increases as shown in Fig. 22.

In the case of square cross-section model, the drag coefficient C_D is set to 1.6, and the inertia coefficient C_M set to 2.186 in order to calculate the fluid force with the use of the modified Morison equation in Eq. (39). Similarly, for the diamond cross-section structure, the drag and the inertia force coefficient are set to 1.5 and 2.194, respectively, and the corresponding parameters are shown in Table 9.

As shown in Fig. 23(a), the maximum free surface elevation of both square and diamond cross-sectional models are observed at $t = 0.5\,s$, and the maximum elevation of the square cross-section model is larger than that of the diamond cross-section model. As shown in Figs 23(b) and (c), the fluid forces exerted on the moving structure are analytically and numerically calculated. After stabilizing the gravitational acceleration ($t = 0.05\,s$), the numerical force increases due to the acceleration of motion and free surface elevation η. After $t = 0.35\,s$, the acceleration of structure decreases to zero as the column moves at a constant speed. In that range, the numerical forces are constantly calculated, and the analytical force calculated with and without η also show the same aspect. The numerical result with the smoothing length factor $\lambda = 1.2$ is slightly larger than the result with $\lambda = 1.1$, and the wave force profile using $\lambda = 1.2$ shows better agreement with the analytical results of the Morison equation.

The optimum value of lambda obtained in Section 4 is employed, and the numerical force converges to the analytical force considering η after 0.6 s. This implies that the number of particles in the numerical model using λ of 1.1 or 1.2 is reasonable and can effectively be used to calculate the fluid force using the contact

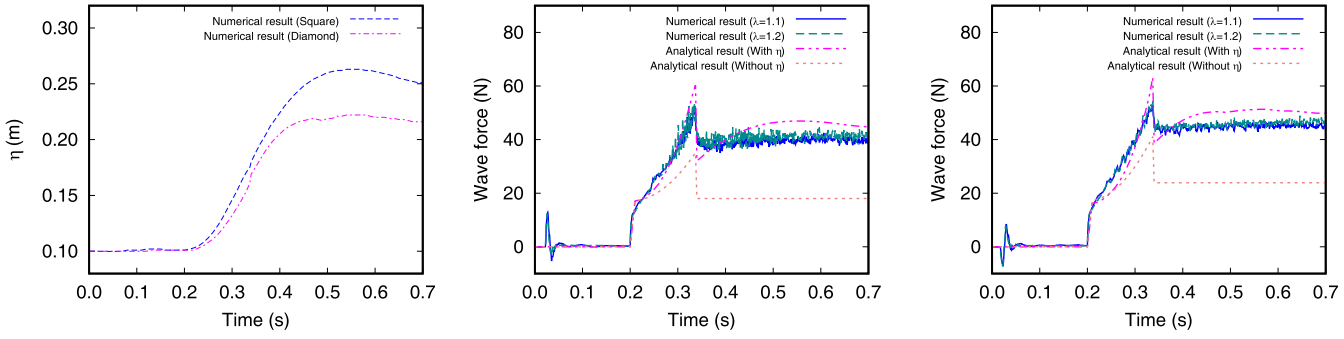

(a) Free surface elevation (b) Square cross-section model (c) Diamond cross-section model

Fig. 23. Analytical and numerical results using Morison equation.

force regardless of the cross-sectional shape of the structure. Using λ greater than 1.2 allows the numerical force to overestimate the fluid force calculated by the Morrison equation and to underestimate the fluid force when using a value smaller than 1.1. Overall, the numerical results show a good agreement compared with the analytical result calculated by the Morison equation considering the η.

6. Conclusions

In this study, the Smoothed Particle Hydrodynamics (SPH) method is coupled with the conventional Finite Element Method (FEM) to simulate the wave forces of open surface flow. To calculate the force accurately, the effects of the initial particle spacing and the smoothing length factor λ are investigated, and the optimal parameters are obtained by comparing the numerical results with available experiment data and analytical formulas.

In order to describe the fluid-structure interaction, the fluid is modeled with smoothed particles while the structure is discretized with conventional 8-node solid finite elements. The contact condition is imposed between the fluid particles and the outer surfaces of finite elements to calculate the exerted force on the structure's surfaces by fluid. The root mean square of the difference between the simulation results and the experiment data are investigated to find optimal parameters in terms of the initial spacing and smoothing length factor. Through the simulations, the Gruneisen equation of state is used to define the development of the pressure.

With the use of the node-to-surface contact algorithm, the water pressure is reproduced using the SPH method for the water column on an elastic plate. A sidewall of the tank is modeled with a finite element, and the applied force by the fluid particles is summed up. The numerical results show a good agreement with the analytical results, and however, the difference of the smoothing length factor λ and the time step scale factor β show little difference in the results.

The dam-break simulation results available in the literature, compared with the experiment results, often overestimate the peak interaction force. Parametric studies are carried out by changing the particle spacing and the smoothing length parameter, respectively. With rough initial spacings, the hydrodynamic forces by SPH particles are estimated to be larger than the experiment result, and the force profile is jagged. With the fine discretization with 5 mm spacing, the results are more accurate than the results from rougher spacings. By changing the smoothing length factor λ, the overall error increases if the length parameter λ is smaller than 1.1 or larger than 1.2. Therefore, the value between 1.1 and 1.2 is recommended to obtain accurate solutions.

With the optimal values of parameters, the accuracies of simulations are validated by solving numerical problems. By moving the solid column modeled with a various cross-section in the fluid, the analytical force acting on the structure's surface is calculated, and the force is compared with the simulation results. Overall, the numerical result shows good agreement with the analytical result if the elevation η is incorporated.

To simulate the fluid-structure interaction, we investigate the effectiveness of the SPH method coupled with FEM, and the results prove the accuracy of the simulation technique. The SPH-FEM coupled fluid-structure interaction simulation is very useful because the SPH particles can describe large deformation and break of waves without imposing any remeshing and artificial conditions.

The numerical results of hydrodynamic pressure on an elastic plate and dam-break examples using SPH-FEM couplings show that hydrostatic and hydrodynamic forces can be accurately calculated by using the contact force. Also, from the numerical results in Section 5, it is possible to estimate the force where a constant current acts on a fixed structure and where a regular wave with a long wavelength acts on the structure. These imply that the numerical simulation technique developed in the present work can effectively be used to design the offshore structures including ocean research station and marine transportation such as a ship. The parameters obtained in the present study will be beneficial to solve the fluid-structure interaction requiring the accurate calculation of the hydrostatic and hydrodynamic force.

Acknowledgement

This work was supported by the National Research Foundation of Korea (NRF) grant funded by the Korea government (Ministry of Science and ICT) (No. 2017R1A5A1014883), and was also a part of the project titled “Construction of Ocean Research Station and their Application Studies” funded by the Ministry of Oceans and Fisheries, Korea.

References

Acrylic, Plaxiglas G., 2013. Sheet, Tech. Rep. Arkema group technical report.
Arnason, H., 2005. Interactions between an Incident Bore and a Free-Standing Coastal Structure. Ph.D. thesis. University of Washington.
Arroyo, M., Ortiz, M., 2006. Local maximum-entropy approximation schemes: a seamless bridge between finite elements and meshfree methods. Int. J. Numer. Methods Eng. 65 (13), 2167–2202.
Attaway, S., Heinstein, M., Swegle, J., 1994. Coupling of smooth particle hydrodynamics with the finite element method. Nucl. Eng. Des. 150 (2), 199–205.
Barreiro, A., Crespo, A.J.C., Domínguez, J.M., Gómez-Gesteira, M., 2013. Smoothed particle hydrodynamics for coastal engineering problems. Comput. Struct. 120, 96–106.
Bathe, K.J., 2006. Finite Element Procedures.
Bea, R., Xu, T., Stear, J., Ramos, R., 1999. Wave forces on decks of offshore platforms. J. Waterw. Port, Coast. Ocean Eng. 125 (3), 136–144.
Boyd, R., Royles, R., El-Deeb, K., 2000. Simulation and validation of undex phenomena relating to axisymmetric structures. In: 6th International LS-DYNA Users Conference Simulation, pp. 9–11.
Chella, M.A., Tørum, A., Myrhaug, D., 2012. An overview of wave impact forces on offshore wind turbine substructures. Energy Procedia 20, 217–226.
Chun, I., Woo, C., Navaratnam, C.U., Shim, J., 2016. Design wave condition and structural analysis for jacket structures installed in wave breaking zone. In: The 26th International Ocean and Polar Engineering Conference. International Society of Offshore and Polar Engineers.
Clauss, G., Lehmann, E., Ostergaard, C., 1992. Offshore Structures - Conceptual Design and Hydromechanics, vol. 1. Springer.
Crespo, A.J.C., Gómez-Gesteira, M., Dalrymple, R.A., 2007. Boundary conditions generated by dynamic particles in SPH methods. Comput. Mater. Continua (CMC) 5 (3), 173–184.
Cruz, A.M., Krausmann, E., 2008. Damage to offshore oil and gas facilities following hurricanes katrina and rita: an overview. J. Loss Prev. Process. Ind. 21 (6), 620–626.
Cummins, S.J., Silvester, T.B., Cleary, P.W., 2012. Three–dimensional wave impact on a rigid structure using smoothed particle hydrodynamics. Int. J. Numer. Methods Fluids 68 (12), 1471–1496.
Dalrymple, R.A., Knio, O., 2001. Sph modelling of water waves. In: Proceedings of 4th Conference on Coastal Dynamics, vol. 01. ASCE, pp. 779–787.
Fourey, G., Hermange, C., Le Touzé, D., Oger, G., 2017. An efficient fsi coupling strategy between smoothed particle hydrodynamics and finite element methods. Comput. Phys. Commun. 217, 66–81.
Gigold, R.A., Monaghan, J.J., 1977. Smoothed particle hyrodynamics: theory and application to non spherical star. Mon. Not. R. Astron. Soc. 181 (3), 375–389.
Gómez-Gesteira, M., 2013. SPHERIC SPH Benchmark Test Cases: Test 1-force Exerted by a Schematic 3D Dam Break on a Square Cylinder.
Gómez-Gesteira, M., Dalrymple, R.A., 2004. Using a three-dimensional smoothed particle hydrodynamics method for wave impact on a tall structure. J. Waterw. Port, Coast. Ocean Eng. 130 (2), 63–69.
Gómez-Gesteira, M., Crespo, A.J.C., Rogers, B.D., Dalrymple, R.A., Dominguez, J.M., Barreiro, A., 2012. Sphysics – development of a free-surface fluid solver – part 2: efficiency and test cases. Comput. Geosci. 48, 300–307.
Gotoh, H., Khayyer, A., 2018. On the state-of-the-art of particle methods for coastal and ocean engineering. Coast Eng. J. 60 (1), 79–103.
Grimaldi, A., Benson, D., Marulo, F., Guida, M., 2011. Steel structure impacting onto water: coupled finite element-smoothed-particle-hydrodynamics numerical modeling. J. Aircr. 48 (4), 1299–1308.
Hallquist, J.O., 2006. LS-DYNA Theory Manual.
Hallquist, J.O., 2007. Ls-dyna Keyword User's Manual. Livermore Software Technology Corporation.
Hong, J.W., Bathe, K.J., 2005. Coupling and enrichment schemes for finite element and finite sphere discretizations. Comput. Struct. 83 (17–18), 1386–1395.

Johnson, G.R., Beissel, S.R., 1996. Normalized smoothing functions for sph impact computations. Int. J. Numer. Methods Eng. 39 (16), 2725–2741.
Kettle, A.J., 2015. Storm britta in 2006: offshore damage and large waves in the north sea. Natural Hazards & Earth System Sciences Discussions 3 (9).
Khayyer, A., Gotoh, H., Falahaty, H., Shimizu, Y., 2018. An enhanced isph–sph coupled method for simulation of incompressible fluid–elastic structure interactions. Comput. Phys. Commun. 232, 139–164.
Khayyer, A., Gotoh, H., Falahaty, H., Shimizu, Y., 2018. Towards development of enhanced fully-Lagrangian mesh-free computational methods for fluid-structure interaction. J. Hydrodyn. 30 (1), 49–61.
Khayyer, A., Tsuruta, N., Shimizu, Y., Gotoh, H., 2019. Multi-resolution mps for incompressible fluid-elastic structure interactions in ocean engineering. Appl. Ocean Res. 82, 397–414.
Koshizuka, S., Oka, Y., 1996. Moving-particle semi-implicit method for fragmentation of incompressible fluid. Nucl. Sci. Eng. 123 (3), 421–434.
Lee, J., Liu, W., Hong, J.-W., 2016. Impact fracture analysis enhanced by contact of peridynamic and finite element formulations. Int. J. Impact Eng. 87, 108–119.
Li, Z., Leduc, J., Nunez-Ramirez, J., Combescure, A., Marongiu, J.-C., 2015. A non-intrusive partitioned approach to couple smoothed particle hydrodynamics and finite element methods for transient fluid-structure interaction problems with large interface motion. Comput. Mech. 55 (4), 697–718.
Libersky, L.D., Petschek, A.G., Carney, T.C., Hipp, J.R., Allahdadi, F.A., 1993. High strain Lagrangian hydrodynamics: a three-dimensional sph code for dynamic material response. J. Comput. Phys. 109 (1), 67–75.
Liu, W., Hong, J.W., 2012. Discretized peridynamics for linear elastic solids. Comput. Mech. 50 (5), 579–590.
Liu, W., Hong, J.W., 2012. Discretized peridynamics for brittle and ductile solids. Int. J. Numer. Methods Eng. 89 (8), 1028–1046.
Liu, W., Hong, J.W., 2012. A coupling approach of discretized peridynamics with finite element method. Comput. Methods Appl. Mech. Eng. 245, 163–175.
Liu, M.B., Liu, G.R., 2010. Smoothed particle hydrodynamics (SPH): an overview and recent developments. Arch. Comput. Methods Eng. 17 (1), 25–76.
Lucy, L.B., 1977. A numerical approach to the testing of the fission hypothesis. Astron. J. 82 (12), 1013.
Monaghan, J.J., 1994. Simulating free surface flows with sph. J. Comput. Phys. 110, 399–406.
Monaghan, J.J., Kos, A., 1999. Solitary waves on a cretan beach. J. Waterw. Port, Coast. Ocean Eng. 125 (3), 145–154.
Morison, J.R., O'brien, M.P., Johnson, J.W., 1950. The force exerted by surface waves on piles. J. Pet. Technol. 2 (5), 149–154.
Roque, C., Ferreira, A., Reddy, J., 2011. Analysis of timoshenko nanobeams with a nonlocal formulation and meshless method. Int. J. Eng. Sci. 49 (9), 976–984.
Sarpkaya, T., 2010. Wave Forces on Offshore Structures. Cambridge university press.
Silvester, T.B., Cleary, P.W., 2006. Wave-structure interaction using smoothed particle hydrodynamics. In: Fifth International Conference on CFD in the Process Industries, pp. 13–15.
Sumer, B.M., Fredsøe, J., 2006. Hydrodynamics Around Cylindrical Structures (Revised Edition) 26.
Vandiver, J.K., et al., 1977. Detection of structural failure on fixed platforms by measurement of dynamic response. J. Pet. Technol. 29 (3), 305–310.
Vuyst, T.D., Vignjevic, R., Campbell, J., 2005. Coupling between meshless and finite element methods. Int. J. Impact Eng. 31 (8), 1054–1064.
Wang, L., Khayyer, A., Gotoh, H., Jiang, Q., Zhang, C., 2019. Enhancement of pressure calculation in projection-based particle methods by incorporation of background mesh scheme. Appl. Ocean Res. 86, 320–339.